

Cosmic ray energy reconstruction from the $S(500)$ observable recorded in the KASCADE-Grande air shower experiment



W.D. Apel^a, J.C. Arteaga-Velázquez^b, K. Bekk^a, M. Bertaina^c, J. Blümer^{a,d}, H. Bozdog^a, I.M. Brancus^e, E. Cantoni^{c,f,1}, A. Chiavassa^c, F. Cossavella^{d,2}, K. Daumiller^a, V. de Souza^g, F. Di Piero^c, P. Doll^a, R. Engel^a, D. Fuhrmann^{h,3}, A. Gherghel-Lascu^e, H.J. Gils^a, R. Glasstetter^h, C. Grupenⁱ, A. Haungs^{a,*}, D. Heck^a, J.R. Hörandel^j, D. Huber^d, T. Huege^a, K.-H. Kampert^h, D. Kang^d, H.O. Klages^a, K. Link^d, P. Łuczak^k, H.J. Mathes^a, H.J. Mayer^a, J. Milke^a, B. Mitrica^e, C. Morello^f, J. Oehlschläger^a, S. Ostapchenko^l, N. Palmieri^d, M. Petcu^e, T. Pierog^a, H. Rebel^a, M. Roth^a, H. Schieler^a, S. Schoo^a, F.G. Schröder^a, O. Sima^m, G. Toma^{e,*}, G.C. Trincherio^f, H. Ulrich^a, A. Weindl^a, J. Wochele^a, J. Zabierowski^k

^a Institut für Kernphysik, KIT – Karlsruhe Institute of Technology, Germany

^b Universidad Michoacana de San Nicolás de Hidalgo, Inst. Física y Matemáticas, Morelia, Mexico

^c Dipartimento di Fisica, Università degli Studi di Torino, Italy

^d Institut für Experimentelle Kernphysik, KIT – Karlsruhe Institute of Technology, Germany

^e Horia Hulubei National Institute of Physics and Nuclear Engineering, Bucharest, Romania

^f Osservatorio Astrofisico di Torino, INAF Torino, Italy

^g Universidade São Paulo, Instituto de Física de São Carlos, Brazil

^h Fachbereich Physik, Universität Wuppertal, Germany

ⁱ Department of Physics, Siegen University, Germany

^j Department of Astrophysics, Radboud University Nijmegen, The Netherlands

^k National Centre for Nuclear Research, Department of Astrophysics, Łódź, Poland

^l Frankfurt Institute for Advanced Studies (FIAS), Frankfurt am Main, Germany

^m Department of Physics, University of Bucharest, Bucharest, Romania

ARTICLE INFO

Article history:

Received 21 April 2015

Revised 9 November 2015

Accepted 14 December 2015

Available online 19 December 2015

Keywords:

$S(500)$

Cosmic ray

Hadronic interaction model

KASCADE-Grande

Primary energy

ABSTRACT

The energy reconstruction at KASCADE-Grande is based on a combination of the shower size and the total muon number, which are both estimated for each individual air shower event. We present investigations where we employed a second method to reconstruct the primary energy using $S(500)$, which are the charged particle densities inferred with the KASCADE-Grande detector at a distance of 500 m from the shower axis. We considered the attenuation of inclined showers by applying the “Constant Intensity Cut” method and we employed a simulation-derived calibration to convert the recorded $S(500)$ into primary energy. We observed a systematic shift in the $S(500)$ -derived energy compared with previously reported results obtained using the standard reconstruction technique. However, a comparison of the two methods based on simulated and measured data showed that this shift only appeared in the measured data. Our investigations showed that this shift was caused mainly by the inadequate description of the shape of the lateral density distribution in the simulations.

© 2015 Elsevier B.V. All rights reserved.

1. Introduction

Experimental studies of cosmic rays are mainly concerned with inferring the arrival direction, the energy spectrum, and the elemental composition of primary cosmic radiation. The primary energy spectrum falls steeply and extends up to 10^{20} eV. Two features are clearly visible in the spectrum in the form of two spectral index changes. These features produce a spectrum shape similar to

* Corresponding authors.

E-mail addresses: andreas.haungs@kit.edu (A. Haungs), gabriel.toma@outlook.de (G. Toma).

¹ Present address: Istituto Nazionale di Ricerca Metrologia, INRIM, Torino, Italy.

² Present address: DLR Oberpfaffenhofen, Germany.

³ Present address: University of Duisburg-Essen, Duisburg, Germany.

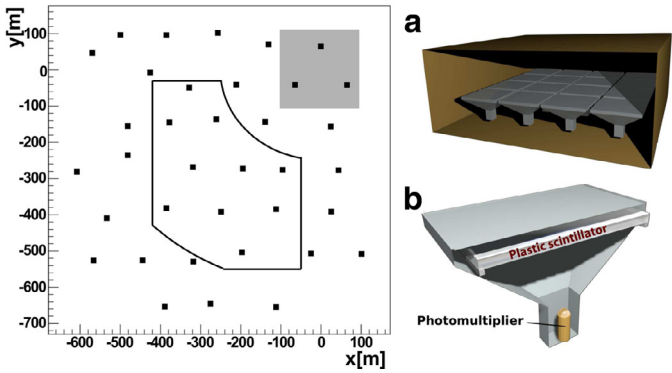


Fig. 1. *Left:* schematic top view of the KASCADE-Grande detector array (the Grande stations are shown as square dots and the fiducial area by the line contour; see the text) and the area covered by KASCADE (shaded rectangle); *right (a)* simplified three-dimensional view of the inside of a Grande station; *right (b)* internal view of a scintillator module.

a bent human leg, and thus they are referred to as *knee* (steepening of the spectrum) and *ankle* (flattening). These two features are strongly correlated in models for describing their source (e.g., [1,2]). In general, it is accepted that toward the highest energies ($E_0 > 5 \times 10^{18}$ eV), the component above the ankle is most likely to be of extragalactic origin [3]. Toward the lower energies (i.e., $E_0 \approx 4 \times 10^{15}$ eV), the knee is caused by the rigidity-dependent extinction of the light component in the galactic radiation.

The KASCADE-Grande [4] experiment was designed to record extensive air showers (EAS) in the 10^{16} – 10^{18} eV energy range to address questions regarding the transition to extragalactic radiation. Recent results obtained by KASCADE-Grande [7] showed that the flux of cosmic rays is in very good agreement with the results of other experiments (e.g., KASCADE [5], EAS-TOP [6]). The all-particle energy spectrum determined by KASCADE-Grande exhibits a hardening of the spectrum at 2×10^{16} eV, a knee-like feature at around $10^{16.92}$ eV due to heavy primaries, and an ankle-like hardening at $10^{17.08}$ eV due to the light component [7–9]. These results were obtained by a reconstruction technique based on an N_{ch} – N_μ correlation (i.e., total shower size – muon size) to infer the primary energy from the data recorded by KASCADE-Grande.

In this study, we present a second approach for reconstructing the primary energy obtained using KASCADE-Grande. We applied this approach independently of the standard method and to the same shower sample, thereby facilitating subsequent cross-checks of the results. The new method is based on a specific primary energy estimator, i.e., the attenuation-corrected charged particle density at a distance of 500 m from the shower axis, $S(500)$. The interest in this observable (i.e., the signal at a fixed radial distance) is particularly justifiable for a loosely spaced detector array such as AGASA [10], where the total shower size cannot be evaluated on an event-by-event basis (although this is not the case in the KASCADE-Grande experiment).

2. KASCADE-Grande

The KASCADE-Grande [4] detector array was situated at the site of the Karlsruhe Institute of Technology – KIT, Campus North, Germany (49° N, 8° E) at 110 m a.s.l. It had a roughly rectangular shape with a length of 700 m (Fig. 1 left) and it comprised a multi-detector system. Several types of detectors enabled the measurement of different extensive air shower (EAS) observables. The research described in this study was based on measurements of the lateral distribution of charged particle densities in EAS.

Historically, the KASCADE-Grande detector was an extension of a smaller array, the KASCADE [5], which operated from 1996. KASCADE was a complex detector that aimed to clarify the origin of the knee in the primary energy spectrum. Thus, it was

designed to record air showers initiated by primaries with energies in the 10^{14} – 10^{16} eV range. KASCADE was designed to record numerous observables associated with the electromagnetic, muonic, and hadronic EAS components.

The decision to extend the KASCADE array was motivated by the need to expand EAS observations toward primary energies in the 10^{16} – 10^{18} eV range, thereby focusing on the expected transition from galactic to extragalactic cosmic rays. In particular, measurements in this energy range could clarify whether a second knee-like structure exists in the energy spectrum. However, recording higher energy air showers presented specific challenges, which guided the extension of KASCADE to KASCADE-Grande. EASs initiated by higher energy primaries contain more particles and they cover a wider area at the observation level. These showers tend to saturate the detectors close to the shower core. Furthermore, in order to better describe larger events, it is necessary to sample information from a wider radial range in the lateral particle density distributions. Another issue is that larger EAS events (produced by higher energy primaries) occur less frequently. The solution was to expand the sensitive area of the existing detector by installing an additional array (the Grande array) with an increased spacing between stations and by covering a wider area, thereby creating KASCADE-Grande.

The Grande array comprised 37 detector stations (formerly part of the EAS TOP array [6]), which were arranged on the ground in a roughly hexagonal grid with a spacing of about 140 m (Fig. 1 left). Each station comprised a metal hut housing 16 plastic scintillation detectors organized in a 4×4 pattern (Fig. 1a). Each scintillator was 80×80 cm² wide and 4 cm thick, and it was enclosed by a pyramidal steel casing (Fig. 1b). The scintillator was viewed from below by a high gain photo-multiplier. The four central modules in each station were also equipped with low gain photomultipliers. The total effective area was 10 m² per station.

KASCADE-Grande was in operation from 2003 until 2013, after which it was dismantled.

3. Reconstruction of $S(500)$

3.1. $S(500)$ as an energy estimator

Previous studies have shown that the charged particle density in air showers becomes independent of the primary mass at a large but fixed distance from the shower axis, and that it can be used as an estimator for the primary energy [11]. According to a comparison of p and Fe initiated showers, the $e^{+/-}$ excess in p showers diminish toward lower radial ranges as the distance to the shower axis increases because the electrons are absorbed. In addition, the muon excess in the Fe showers gradually becomes more important at larger radial ranges. Based on this trend, for a given radial range, this behavior produces overlapping of the lateral distributions (Fig. 2) and the value of the charged particle density becomes mass independent in that location. This distance is specific for a given experiment because it depends on the observation level as well as on the detector threshold and the sensitivity to the charged particle component. Based on this property, a method was derived to reconstruct the primary energy from the particular value of the charged particle density observed at specific radial distances. In the AGASA experiment, this technique was applied at a distance of 600 m to the shower axis [10]. For the KASCADE-Grande array, detailed simulations [12] have shown that the particular distance at which this effect occurs is about 500 m (Fig. 2); hence, the notation $S(500)$ for the charged particle density at a distance of 500 m from the shower axis. The distance is measured on a plane normal to the shower axis and containing the shower core. The property of mass independence is also visible in Fig. 3, which shows the correlation between the energy estimator $S(500)$ and the primary energy for different primary masses.

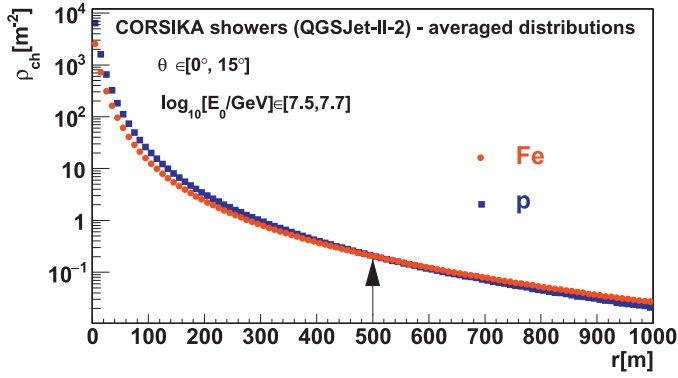


Fig. 2. Averaged simulated lateral distributions for the p and Fe primaries with energy in a narrow range.

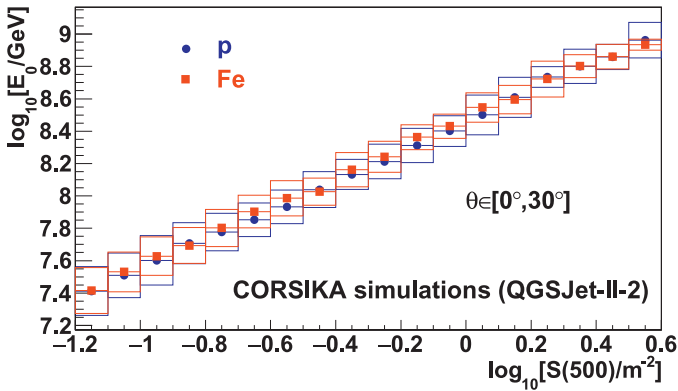


Fig. 3. Dependence of the primary energy E_0 on the $S(500)$ for p and Fe primaries (simulated showers with fairly equal proportions for the two masses), where the boxes show the spread of data and the errors on the mean are dot-sized.

It must be stressed that the properties of the $S(500)$ observable have been predicted by simulation studies based on the QGSJet-II-2 [14] hadronic interaction model and it is entirely possible that simulations based on other interaction models could predict different mass-independent observables. However, tests have shown that in the case of KASCADE-Grande, the $S(500)$ remains usable [17] with other models such as EPOS 1.99 [18], QGSJet-II-4 [19], and EPOS-LHC [20].

3.2. Event selection

Simulated showers are used for fine tuning the reconstruction procedure as well as for calibrating the observable of interest, $S(500)$ with the primary energy. We applied the analysis in an identical manner to simulated and experimental events using the same reconstruction procedure.

We simulated air showers using the CORSIKA [13] Monte Carlo EAS simulation tool, with the QGSJet-II-2 [14] and FLUKA [15,16] models embedded. A thinning procedure was not applied. The set of simulated showers included events simulated for five primaries (p, He, C, Si, and Fe in fairly equal proportions) with a continuous energy spectrum between 10^{15} and 3×10^{18} eV, and with a spectral index $\gamma = -2$ that was harder than the measured data. The harder spectral index allowed a faster increase in the statistical accuracy at higher energies by not simulating as many showers at lower energies compared with a $\gamma \approx -3$ sample. The spectral index obtained from simulations is significantly different from the experimentally observed index, so a weighting was applied to simulated events in most subsequent studies to emulate a softer energy spectrum $\gamma = -3$. About 3×10^5 events were simulated for each primary. The arrival direction of showers was isotropical and the shower cores were spread randomly on an area larger than the

Grande array. In addition, smaller sets of showers were simulated in comparisons using the high energy hadronic interaction models EPOS 1.99, QGSJet-II-4, and EPOS-LHC.

To select a high quality shower sample, a set of quality cuts was applied in an identical manner to the simulated events and to the data. The fiducial area (as shown in Fig. 1) was set the same as that in [7] in order to increase the similarity of the selected shower samples for both reconstruction approaches. The fiducial area was a rectangle, where we omitted the nearest and farthest corners relative to the KASCADE array in order to minimize under- and over-estimation of the muon number, which is important for the standard reconstruction approach [7]. In the present study, at least 25 triggered stations were required in every event. For a station to be valid, it had to provide trigger time information and be correlated with the event within a given time window. Another quality cut considered the zenith angle of incidence, which was limited to up to 30° . This condition was intended to minimize geometrical effects due to shower inclinations and to reduce the fraction of showers with no information in the lateral density distribution at large radial ranges. Following these quality cuts and considering the chosen fiducial area, there were 28 triggered stations on average in each event. About half of all the events had recorded data at 500 m. Thus, most of the triggered stations were less than a distance of 500 m from the shower axis. The acceptance of the experiment under the aforementioned assumptions for the fiducial area and zenith angle was 1.28×10^5 m² sr. The total acquisition time was 1503 days, thereby leading to an exposure of 1.66×10^{13} m² s sr.

3.3. Reconstruction of $S(500)$

The reconstruction procedure described in the following was applied without any changes to both the simulated and experimental events [21].

The KASCADE-Grande detector stations recorded the energy deposits of particles and associated temporal information (arrival times of particles) without disentangling the particle type (e.g., muons from electrons). The temporal information was used to reconstruct the zenith and azimuth angles of the shower axis [22]. The recorded energy deposit was converted into particle densities using appropriate lateral energy correction functions (LECF) [23] while considering the arrival direction of the shower and the azimuthal position of each station around the shower axis.

For both the experimental and simulated events, the energy deposit information is usually given in the detector plane. However, the particle densities were reconstructed in the plane normal to the shower axis [24] because the shower properties were more clearly elucidated in this plane. In order to project the shower information from the detector plane onto the normal plane, special care was taken to avoid its distortion. For an inclined shower, the particle density around the shower core at a given radial range can vary due to differences in particle absorption and scattering in the atmosphere. A relevant example is the case of particles in the lower half of the EAS particle front compared with those in the upper half for an inclined shower. The particles in the lower part of the EAS front will travel a shorter distance through the atmosphere before reaching the detector level. If the detectors are placed predominantly under the shower axis, then the particle density would be overestimated (in the opposite case, the density would be underestimated). Furthermore, the angle of incidence of particles in detectors would be different in the two cases because the particles have a transverse momentum and they do not propagate parallel to each other or to the shower axis. The error in the density affects both the reconstructed shower size and the accuracy of shower core reconstruction. Therefore, we introduced a procedure to compensate for the attenuation of inclined showers. In addition,

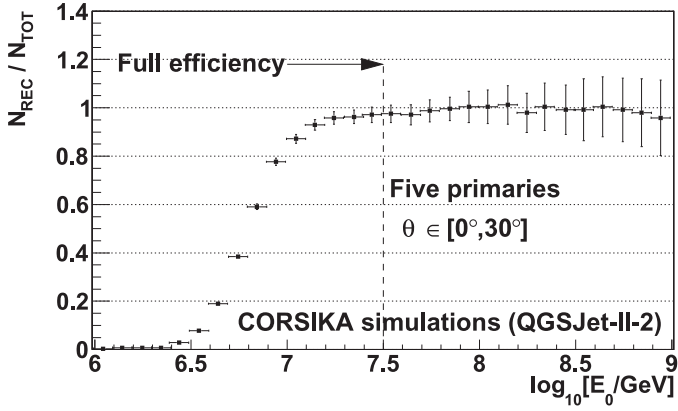


Fig. 4. Ratio of the number of simulated events where the $S(500)$ was successfully reconstructed relative to the total number of simulated events as a function of the primary energy (the energies of the simulated events are distributed as a power law with spectral index $\gamma = -2$).

we considered the dependence of energy deposits on the angle of incidence for the particles.

To calculate the charged particle density at distance of 500 m from the shower axis, the lateral density distribution was approximated with a three-parameter Linsley function (Eqs. (1) and (2)) [25] (in the analysis, we excluded information within a small radial range around the shower core to avoid effects introduced by saturated stations)⁴:

$$\rho_{ch} = \frac{N}{r_0^2} \cdot C(\alpha, \eta) \cdot \left(\frac{r}{r_0}\right)^{-\alpha} \cdot \left(1 + \frac{r}{r_0}\right)^{-(\eta-\alpha)}, \quad (1)$$

where

$$C(\alpha, \eta) = \Gamma(\eta - \alpha) \cdot [2\pi \cdot \Gamma(2 - \alpha) \cdot \Gamma(\eta - 2)]^{-1} \quad (2)$$

with

$\rho_{ch}(r)$ – charged particle density at distance r [m] from the shower core;

N – shower size (in this case, the total number of charged particles);

r_0 – Molière type radius [m];

r – radius [m];

α, η – two shape parameters.

The shower core was reconstructed iteratively. In the first approximation, it was obtained as the center of mass of the energy deposits at the stations. Next, this result was refined using a Linsley fit of the lateral distribution, where the α and η parameters were fixed. A similar iterative method was used in the standard reconstruction at KASCADE-Grande. The shower core reconstruction was applied in an identical manner for the data and simulated events.

Fig. 4 shows that the fraction of successfully reconstructed $S(500)$ observables in the simulated events exceeded 95% at around $\log_{10}(E_0/\text{GeV}) = 7.5$. The fluctuations around a value of 1 for the energies $\log_{10}(E_0/\text{GeV}) > 7.5$ were due to the fluctuations in the reconstructed shower cores inside or outside the fiducial area used for shower selection. Approximately 9.05×10^5 experimental events passed all of the imposed selection cuts and the $S(500)$ was reconstructed successfully. In contrast to the $S(500)$ -based method, the full efficiency of the standard reconstruction procedure [7] (based on $N_{ch} - N_{\mu}$) was reached at lower energies, $E_0 \approx 10^{16}$ eV. This was due mainly to the shower selection procedure

⁴ To applying an independent analysis, we also selected a different lateral density function compared with the standard approach. However, previous studies have shown that both functions work equally well when determining $S(500)$ (for both simulated and experimental events).

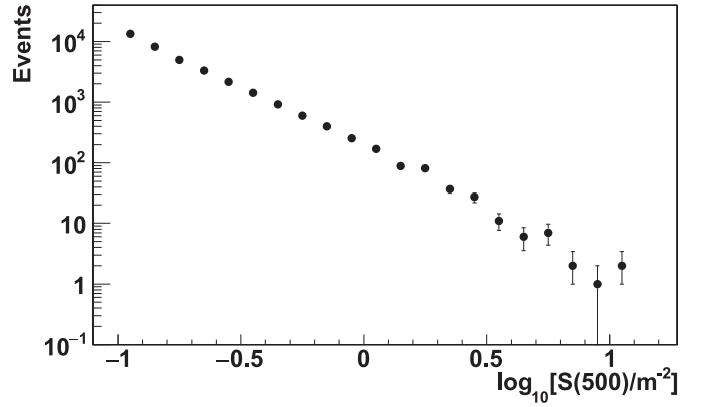


Fig. 5. The measured $S(500)$ spectrum after CIC correction.

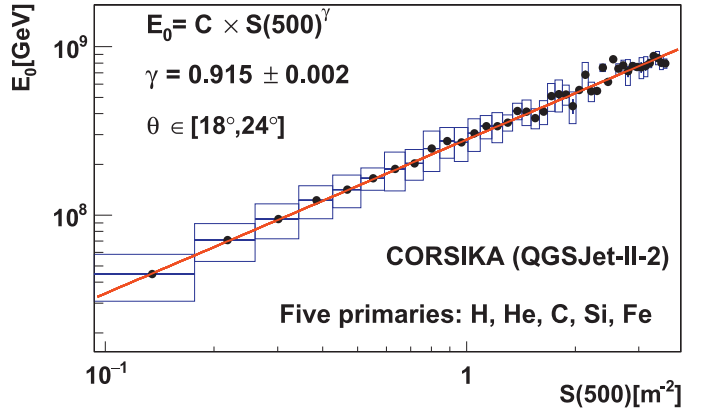


Fig. 6. $E_0 - S(500)$ correlation where the dots represent the profile of the scatter plot with box errors to show the spread of the data and the errors of the mean are dot-sized. The continuous line is a power law fit with $\gamma = 0.915 \pm 0.002$.

(Section 3.2), which was employed to maximize the reconstruction quality of $S(500)$ at the expense of a slight reduction in efficiency.

The recorded $S(500)$ values could not be converted directly into the primary energy without first considering the difference in the attenuation of inclined events in the atmosphere, which was achieved by applying the constant intensity cut (CIC) method to correct all of the recorded $S(500)$ values as if the showers were coming from a fixed zenith angle (Appendix A). The zenith angular distribution in the $0-30^\circ$ peaked at $\approx 21^\circ$, so this value was selected as the CIC reference angle. The measured $S(500)$ spectrum is shown in Fig. 5.

4. Energy reconstruction

4.1. Energy reconstruction using $S(500)$

A calibration was derived from simulated showers with a zenith angle around the CIC reference angle and with a mass composition of five primaries in fairly equal proportions. Fig. 6 shows the calibration obtained using CORSIKA simulations with QGSJet-II-2. The calibrations obtained for the other interaction models were very similar and thus they are not shown. The calibration was a power law function as found in Eq. (3) and it was used to convert all of the attenuation-corrected $S(500)$ values to the corresponding primary energy:

$$E_0 = C \cdot S(500)^\gamma \quad (3)$$

with C – a constant; and γ – the slope index of the power law dependency.

Under the assumptions of the QGSJet-II-2 model, the energy calibration was found to be composition independent. We calculated the energy resolution in order to test the ability of the

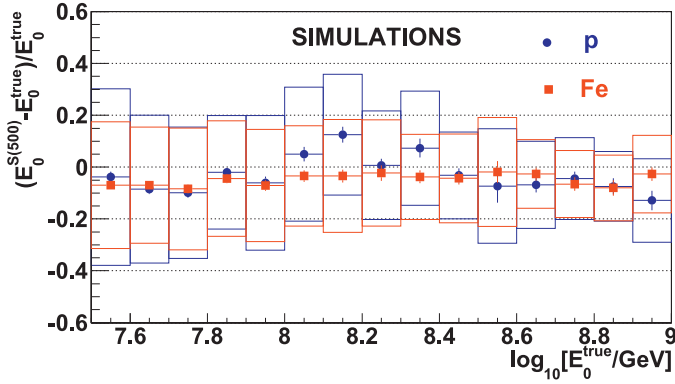


Fig. 7. Energy resolution where the box errors show the spread of the data and the error of the mean with a bar is dot-sized. The plot shows the results for p and Fe primaries, but similar behavior was observed for other primaries.

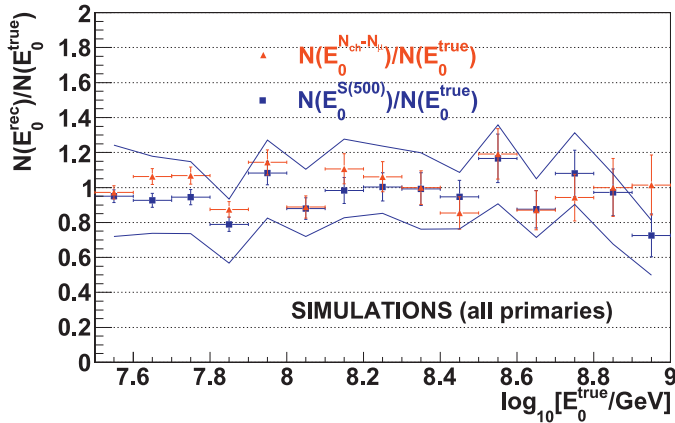


Fig. 8. Bin-by-bin ratio between the reconstructed energy distribution (number of events in each energy bin) and the true energy distribution after reconstructing CORSIKA simulated showers using the two approaches. The continuous lines show the estimated systematic uncertainty for the $S(500)$ -derived distribution (see Appendix C).

method to reproduce the primary energy values. For the simulated shower sample, we show the relative difference between the reconstructed primary energy and the true energy as a function of the primary energy (Fig. 7). The root mean square of the distribution (i.e., the energy resolution) had an overall value of 25% and it improved slightly as the energy increased, which was due to a decrease in the statistical fluctuations in the shower at higher energies. Fig. 7 also shows that there was a slight ($\approx 5\%$) underestimation of the primary energy, which was greater at lower energies but still below 10%. This occurred in the case of small showers where the lateral particle density was very small or there was no data toward $r = 500$ m, and thus the Linsley fit obtained a better description of the range closer to the shower core where it was much steeper. Finally, this led to underestimation of the density value at 500 m.

4.2. Comparison of the results

In order to ensure that the method based on $S(500)$ performed correctly, we evaluated the energy reconstruction using the proposed method and the standard method [7] on an event-by-event basis, first for the simulations and then for the data.

Fig. 8 compares the reconstructed energy spectra obtained using the two methods and the true energy for the same shower sample (in this plot, we show the results obtained by each method relative to the true energy distribution, which we used in the simulations). For simulated showers, we can conclude that both reconstruction methods performed in a similar manner because the

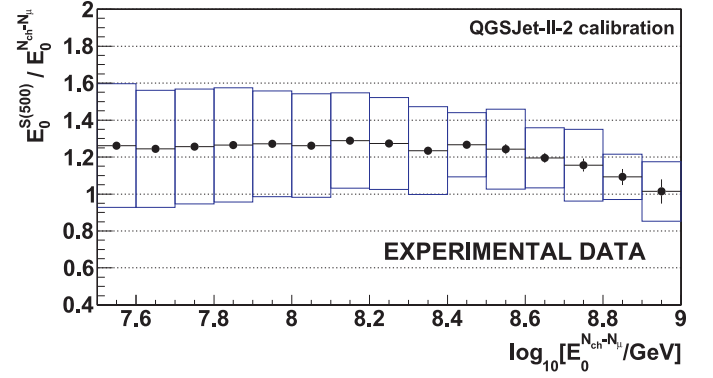


Fig. 9. Ratio of the energy from $S(500)$, $E_0^{S(500)}$ relative to the reconstructed energy using the standard approach, $E_0^{N_{ch}-N_{\mu}}$. The plot shows the profile where box errors indicate the spread of data and the bar errors denote the error of the mean.

results obtained agreed reasonably well with the other. At the highest energy, we found that less events could be reconstructed with the true energy due to the presence of low statistics in the simulated sample.

Next, a similar test was performed using the experimentally recorded data. Fig. 9 plots the ratio of the reconstructed primary energy obtained from the described approach ($E_0^{S(500)}$) relative to that from the standard reconstruction ($E_0^{N_{ch}-N_{\mu}}$) for an experimental shower sample reconstructed using both methods. It can be seen that unlike the simulations in (Fig. 8), for the data, $E_0^{S(500)}$ had systematically higher values (up to 30%) than $E_0^{N_{ch}-N_{\mu}}$. This difference was not constant over the entire accessible energy range and it appeared to diminish at the highest energies above $\log_{10}[E_0^{N_{ch}-N_{\mu}}/\text{GeV}] \approx 8.4$. This was probably due to the variation with energy in the ratio between the electron and muon sizes, which was not reflected in the $S(500)$ value.

The energy spectrum based on the $S(500)$ observable could be determined by applying a correction to the estimated resolution using a response matrix (unfolding). However, we observed a systematic shift in the estimated energy compared with that when the standard method was applied to the KASCADE-Grande detected events, so we investigated the source of this shift. The unfolding procedure, the determination of the spectrum, and a discussion of the uncertainties were described in Appendices B and C.

4.3. Discussion

Given that we used the same procedure to reconstruct both the simulated and experimental data, the disagreement between the two data reconstructions (although they were in good agreement in the simulation) might indicate that certain features of the EAS were not described accurately by the simulations. These features might comprise the shape of the lateral distribution, the shower size, the position of the shower maximum, and the attenuation of the particle number in the atmosphere. Thus, we compared the shower size (N_{ch}) for the p and Fe simulations, as well as for the experimental data, by selecting showers in the same narrow energy range (with the same $S(500)$). For showers detected by KASCADE-Grande in the 10^{16} – 10^{18} eV energy range, we expected that for a given $S(500)$ (i.e., fixed energy), the observed N_{ch} would be in a range delimited by the p and Fe assumptions [1,2]. We used the value of N_{ch} inferred on an event-by-event basis from a modified NKG fit [27] of the lateral distribution, as used in the standard approach [7] (Fig. 10). For various $S(500)$ ranges in Fig. 10, we observed that the data did not satisfy the expectations and they indicated that the mass composition was heavier than Fe. This agreed with the results shown in Fig. 11, which compares the averaged lateral density distributions for the simulated showers

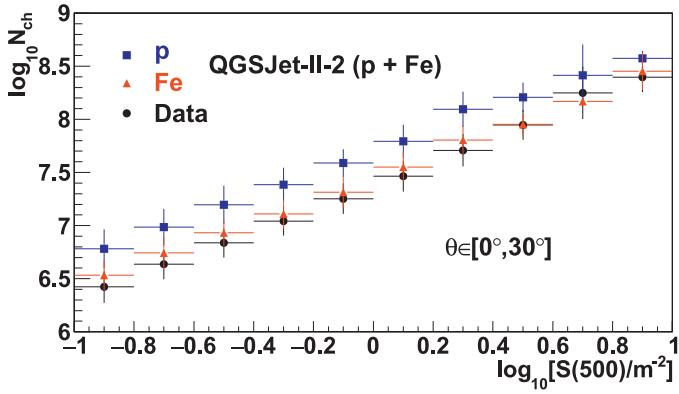


Fig. 10. Correlation between the NKG-derived shower size N_{ch} using the standard approach and the $S(500)$ for p and Fe simulated events, and for the experimental data.

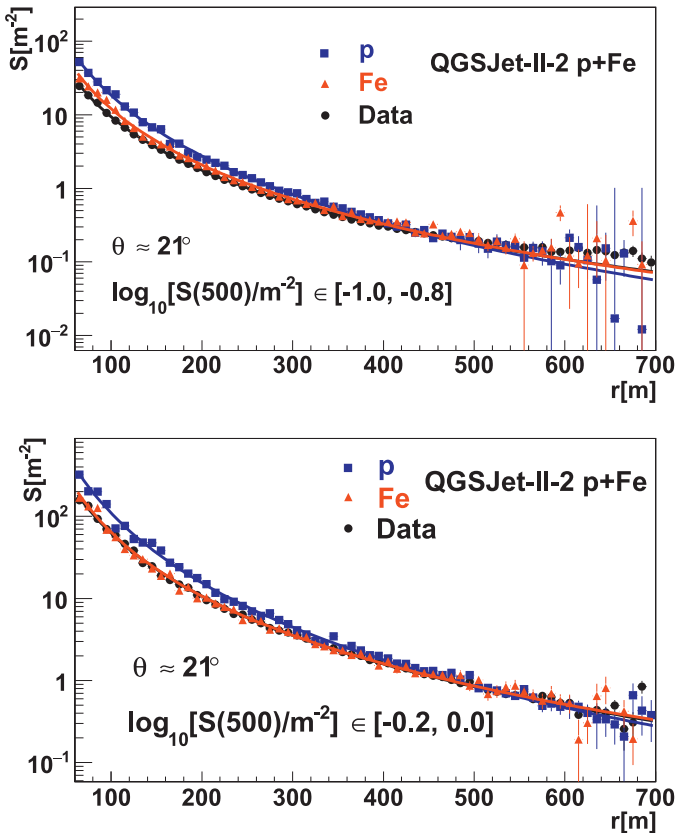


Fig. 11. Averaged lateral charged particle density distributions for the simulations (CORSIKA/QGSJet-II-2 p and Fe showers) and experimental data for events with $\log_{10}[S(500)/m^2] \in [-1.0, -0.8]$ (above) and $\log_{10}[S(500)/m^2] \in [-0.2, 0.0]$ (below). We only show events inclined at $\approx 21^\circ$ to avoid effects induced by attenuation in the atmosphere. The continuous lines are for a Linsley-type function.

(p and Fe primaries) and data. The experimental lateral distribution was outside the p and Fe predictions toward the elements heavier than Fe.

We evaluated this disagreement in more detail. Based on Fig. 10, we imposed a change on an event-by-event basis for the measured $S(500)$ by decreasing the reconstructed $S(500)$ values with a value of $\Delta[\log_{10}S(500)/m^2] = -0.1$. The value -0.1 for this correction was the minimum that had to be introduced in order to satisfy the QGSJet-II-2 (p,Fe) range prediction over the entire energy range accessible to KASCADE-Grande (see Fig. 10). Using the modified experimental $S(500)$ values, the differences in the energy determination vanished at lower energies (Fig. 12) (and the

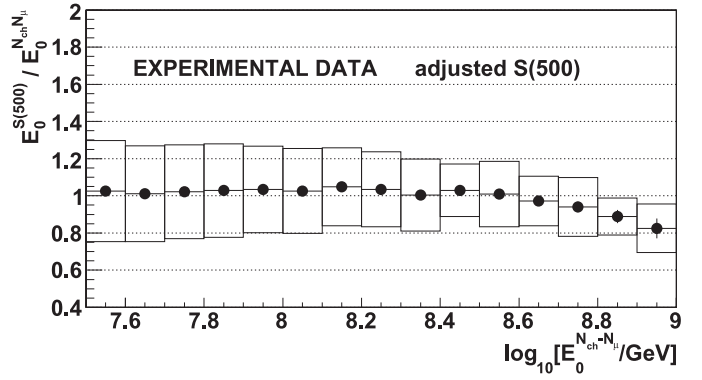


Fig. 12. Ratio between the energy reconstructed from $S(500)$, $E_0^{S(500)}$ and $E_0^{N_{ch}, N_{\mu}}$, where the recorded $S(500)$ was corrected to agree with the QGSJet-II-2 Fe prediction. The box errors show the spread of the data and the bar errors denote the error of the mean.

resulting spectrum was also comparable to that published within the range of the systematic uncertainties, see Appendix C).

Therefore, we concluded that the systematic shift between the two KASCADE-Grande results occurred mainly because the simulations did not accurately describe the shape of the lateral density distributions, where they appear to be excessively steep at large radial ranges compared with the data. The $S(500)$ -based method samples most of its information from a reduced radial range at 500 m from the shower axis, so this method is probably more sensitive to inaccuracies in the shape of the simulated lateral distribution than the standard approach, which samples data from the entire radial range of the lateral density distribution. This is equivalent to saying that a significant (according to Fig. 10, approximately 30% lower density) disagreement in shape at 500 m from the shower axis may have a significantly lower influence on the integrated value N_{ch} . This picture appeared to change at higher energies, where $S(500)$ was already in the steeper part of the lateral distribution. However, the statistics were low, so we could not decide whether 500 m was still an appropriate distance for obtaining an unbiased energy determination.

In the following, we discuss two physics-based possibilities to explain the different lateral shapes of the charged particles in EAS according to the simulations and data.

- The shallower lateral density distribution desired at large radial ranges is consistent with older showers starting higher in the atmosphere, which translates into a larger cross-section for the primary energy. However, this solution appears to contradict the latest results obtained with the Large Hadron Collider (LHC)⁵ [28,29], which do not encourage further increases in the cross-sections in most models. Therefore, an even larger cross-section for the primary does not appear to be a solution that would improve the agreement between the data and simulations.
- In the second approach, it is likely that increasing the muon content at large radial ranges in the simulated showers could have increased the curvature of the lateral distribution given that the ratio N_{μ}/N_{ch} was not constant over the entire radial range in the lateral distribution. At large radial ranges, the electron component is practically extinct and the charge component at such ranges is dominated by muons. Two possible mechanisms for increasing the muon content at large radial ranges are increasing the muon multiplicity (thereby resulting in an overall increase in the number of muons), or increasing the muon lateral spread (which produces a flattening in

⁵ The particle energy of 7 TeV at the LHC translates into a primary energy approximately 3×10^{16} eV that of a proton impinging in the atmosphere.

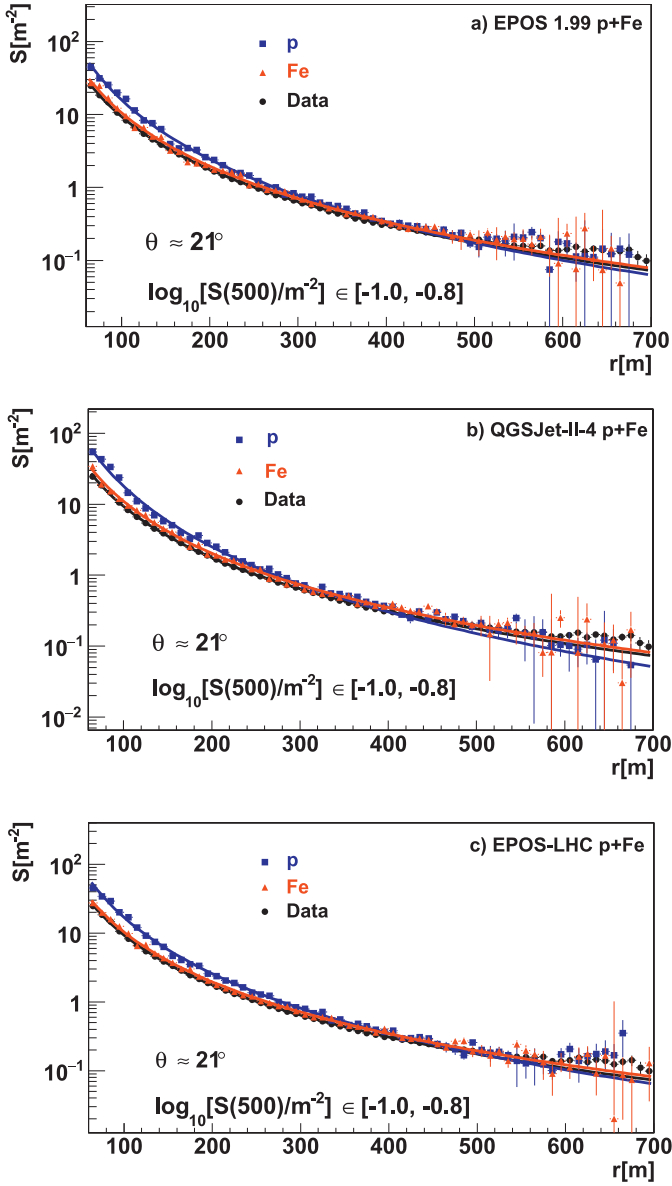


Fig. 13. Averaged lateral charged particle density distributions similar to those in Fig. 11, but in this case, the simulations used the EPOS 1.99 (a), QGSJet-II-4 (b), and EPOS-LHC (c) models.

the lateral distribution but without affecting the muon size). These two mechanisms are not mutually exclusive and they could be combined to some extent. In addition, several other independent studies have shown that the measured muon component appears to be richer than that predicted by simulations (e.g., see [30,31]). A preliminary test of this hypothesis was performed using a set of CORSIKA simulations based on the EPOS 1.99 hadronic interaction model. One of the differences between EPOS 1.99 and QGSJet-II-2 for a given primary is that on average, the EPOS simulated showers will contain more muons (a feature that would clearly affect both reconstruction methods at KASCADE-Grande). Fig. 13a shows the averaged lateral density distributions in a similar manner to Fig. 11, but for simulations based on the EPOS 1.99 model. In addition, Fig. 13b and c shows similar plots for the QGSJet-II-4 and EPOS-LHC hadronic interaction models. With EPOS 1.99, there appeared to be better agreement between the data and simulations, although the experimental data were still not inside the (p, Fe) expected range and the shape was still flatter than that for the simulations.

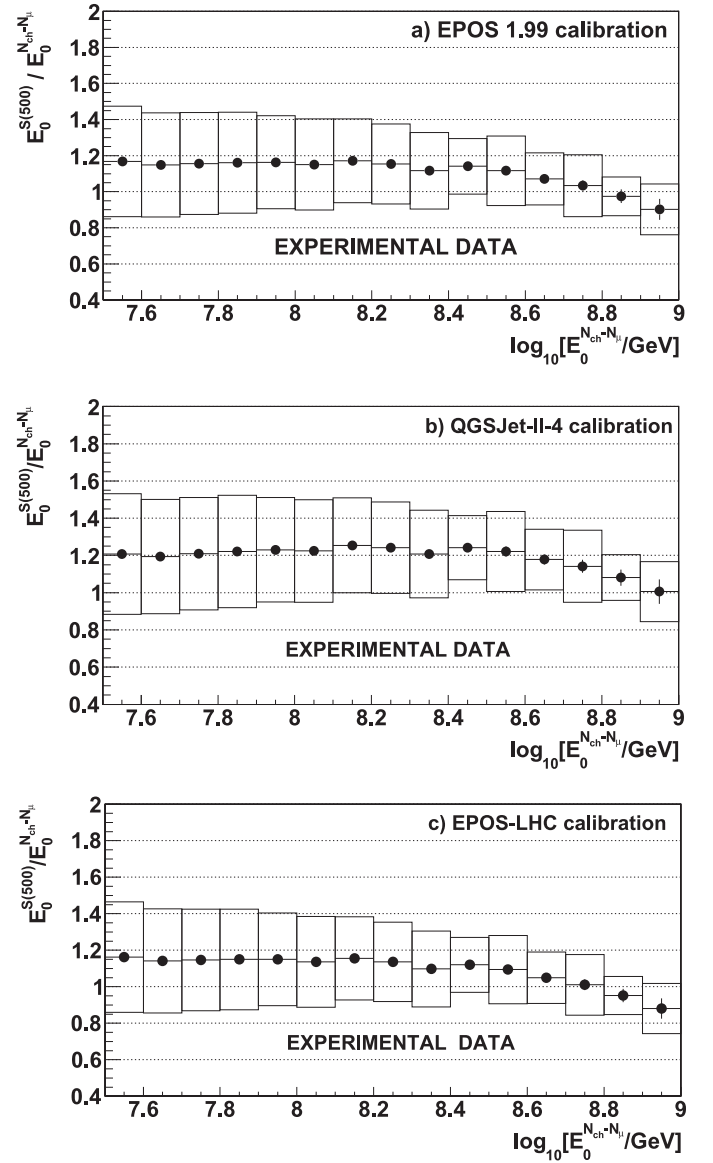


Fig. 14. These plots are similar to that in Fig. 9 but the $S(500)$ -derived energy for KASCADE-Grande was inferred using calibrations based on simulations with EPOS 1.99 (a), QGSJet-II-4 (b), and EPOS-LHC (c).

When we derived the primary energy from $S(500)$ with a calibration based on EPOS 1.99 simulations, there was a systematic 10% decrease in the primary energy compared with that using the QGSJet-II-2 calibration. Thus, the observed discrepancy between the data and simulations was reduced (Fig. 14a), but it did not vanish completely, thereby indicating that simply increasing the muon multiplicity is not a straightforward solution to the problem. The tests with simulated showers based on QGSJet-II-4 and EPOS-LHC showed that these newer models also failed to make significant changes compared with their earlier versions (Figs. 13b, c and 14b, c) for this particular observable. However, a slight improvement could be identified in the post-LHC models compared with earlier versions.

In the $S(500)$ -based method, the simulation-derived calibration is very sensitive to the shape of the simulated lateral distribution and even small deviations in the shapes of the distributions can have significant effects on the resulting energy spectrum. The same is true when we consider the fluctuations in the $S(500)$ observable itself. The detected charge particle density at a distance of 500 m from the shower core could have been accompanied by

significant fluctuations due to the small number of particles per station, or there were no data close to 500 m due to the array size in some cases. However, the sensitivity of this method to the shape of the lateral distribution can be changed into a positive feature when evaluating the simulation quality. In contrast to the $S(500)$ -based approach, the method based on the $N_{ch}-N_{\mu}$ correlation infers the primary energy from the whole range of the lateral distribution and it is affected less by small deviations in the shape, local fluctuations, or a lack of information in the lateral distribution. Therefore, the reconstruction of the primary energy based on the charged particles and muon numbers (shower sizes) is more robust.

5. Conclusions

The primary energy spectrum of cosmic rays in the range of 10^{16} – 10^{18} eV accessible to the KASCADE-Grande experiment was determined based on the correlation between the total number of charged particles and the muon number. In this study, we presented an approach for reconstructing the primary energy of individual measured air showers based on another energy estimator, i.e., the charged particle density at a distance 500 m from the shower axis, which is similar to that used in experiments such as Auger ($S(1000)$ [32]) or AGASA ($S(600)$ [10])⁶. According to the QGSJet-II-2 predictions, the $S(500)$ -derived energy is composition-independent because the density of charged particles at a distance of 500 m to the shower axis is mass-insensitive in the special case of KASCADE-Grande. Thus, we studied simulated events before analyzing experimental data in order to evaluate the reconstruction efficiency and quality, as well as deriving a calibration curve $E_0 - S(500)$. The analysis was applied in an identical manner to the simulated and experimental events.

The $S(500)$ -derived primary energy exhibited a systematic shift compared with the results obtained using the standard reconstruction approach, but only in the case of the measured data. The simulations using both methods obtained energy determinations with similar good quality. We attributed this shift to disagreement between the shape of the simulated lateral distributions and the observed distributions. The simulated lateral distributions were excessively steep at large radial ranges compared with the data. The effect appeared to be much weaker at higher energies, which might be because KASCADE-Grande measured the particle densities only up to a core distance of 700 m, whereas for higher energies, muons dominate the lateral distributions only at larger distances. The inconsistency between the simulations and data was sufficiently large to explain most of the shift in the energy spectra obtained by the two methods. Methodical or detector effects can be excluded from having major effects because several tests were performed, including using different lateral distribution functions, independent analysis codes, and analyzing subsamples of the total shower sample.

We considered two possible solutions to improve the agreement between the data and the simulations. One solution (larger cross-sections) might be less suitable according to recent results obtained at the LHC, but the possible solution of predicting a higher muon multiplicity combined with spatially adjusted (i.e., flatter) muon lateral distributions appears to be more promising, which was supported by the results of preliminary tests based on the EPOS 1.99 and the newer post-LHC interaction models.

Compared with their earlier versions, the QGSJet-II-4 and EPOS-LHC hadronic interaction models did not significantly affect or im-

prove the reconstruction of primary energy based on the $S(500)$ observables.

Acknowledgments

The authors thank the members of the engineering and technical staff of the KASCADE-Grande collaboration, who contributed to the success of the experiment. The KASCADE-Grande experiment was supported in Germany by the BMBF and by the ‘Helmholtz Alliance for Astroparticle Physics – HAP’ funded by the Initiative and Networking Fund of the [Helmholtz Association](#), by the [MIUR](#) and [INAF](#) of Italy, the Polish Ministry of Science and Higher Education, and the Romanian [National Authority for Scientific Research](#), ANCS-UEFISCDI, project numbers [PN-II-ID-PCE-2011-3-0691](#) and [PN-II-RUPD-2011-3-0145](#). G. Toma acknowledges [KIT Karlsruhe](#) for supporting and hosting part of this research activity as well as [DAAD](#) for supporting part of the study in the framework of a doctoral scholarship ([A/06/09016 Ref. 322](#)).

Appendix A. CIC method

Some EAS observables are greatly influenced at the detector level by the zenith angle of the shower because on average, the particles travel along paths with different lengths in the atmosphere depending on the zenith angle. This is the case for the $S(500)$, which on average can have different values for the same primaries (E_0, A_0) arriving from different zenith angles. We need to correct for this effect before performing an analysis simultaneously on all recorded EAS events. This is achieved by applying the CIC method [33]. This method is based on the assumption that for a given minimum primary energy above the full efficiency threshold, we should record the same flux of the primaries (i.e., air showers) from all zenith angles. This is analogous to saying that in the integral spectra from different zenith angles, equal intensity corresponds to the same primary energy.

We performed several CICs on the integral $S(500)$ spectra corresponding to different zenith angles (Fig. A.15) and for each cut we established a correlation between the $S(500)$ and the corresponding zenith angle (Fig. A.16). To build the integral $S(500)$ spectra, we selected the zenith angular intervals from the range $[0^\circ, 30^\circ]$ so that they subtended equal solid angles. We fitted all of the values in Fig. A.16 simultaneously with a functional form derived from a second degree polynomial and we used this functional form as a correction function to account for the attenuation of $S(500)$. All of the reconstructed $S(500)$ values were corrected by bringing them to the value they would have at a chosen reference angle. In the present study, the reference angle was considered

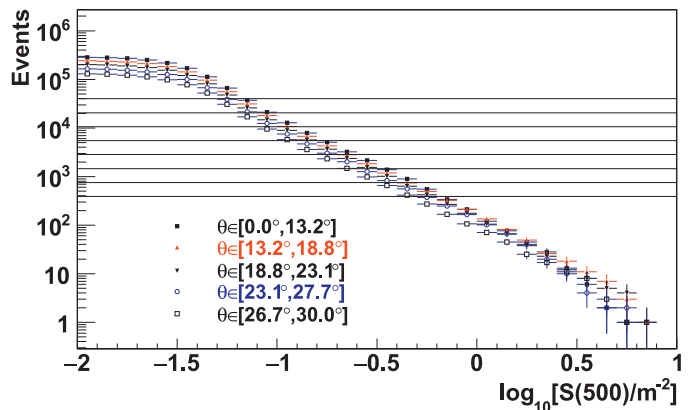


Fig. A.15. Integral $S(500)$ spectra where the horizontal lines are CICs at arbitrarily selected intensities.

⁶ It should be noted that in case of the Auger Observatory, the calibration of the value was based on calorimetric measurements obtained by fluorescence telescopes, whereas simulations were used for AGASA and KASCADE-Grande.

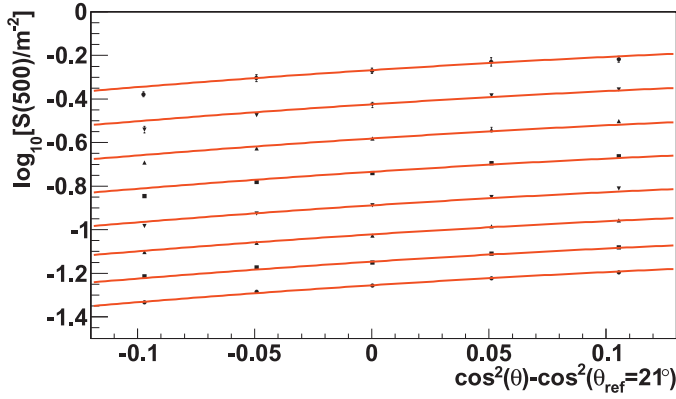


Fig. A.16. Variation in the $S(500)$ observable with the angle of incidence, where each set of points corresponds to a CIC in Fig. A.15. The continuous lines show the global fit of all the points.

to be 21° , since the zenith angular distribution for the recorded EAS sample peaked at this value. The uncertainty associated with each attenuation-corrected $S(500)$ value was derived from the uncertainties in Fig. A.15 by propagating them through the entire calculus of the CIC method (the uncertainty introduced by the global fit in Fig. A.16 was also considered). Thus, the CIC correction was derived entirely from recorded experimental data and it was independent of the simulations.

The attenuation length $\Lambda_{S(500)}$ of $S(500)$ was evaluated using a global fit of the attenuation curves assuming exponential attenuation (Eq. A.1). The resulting value was $\Lambda_{S(500)} = 402 \pm 7 \text{ g cm}^{-2}$.

$$S(500)_\theta = S(500)_0 \cdot \exp\left[\frac{-X_0}{\Lambda_{S(500)}} (\sec\theta - 1)\right] \quad (\text{A.1})$$

with X_0 – the atmospheric depth in g/cm^2 .

Appendix B. Unfolding based on a response matrix

If a given variable is characterized by intrinsic statistical fluctuations, then when representing its spectrum as a histogram with a given bin size, the fluctuations will cause the total value stored in each bin to deviate from the true (unknown) value due to events *leaking* to and from neighboring bins. Therefore, the reconstructed spectrum is obtained from the true spectrum of the given variable by folding the contributions from fluctuations in all neighboring bins in each bin. This migration depends on the bin size and the amount of fluctuations, where its effects can vary greatly depending on the spectral shape. This was the case of the reconstructed energy spectrum, which decreased very steeply. Given the steep decrease in the spectrum, we expected that the contributions to neighboring bins would have a greater effect toward higher energies, where the flux was much lower. This affected the flux value as well as the spectral index, and a correction had to be applied for compensation. This correction was derived using simulated showers and it was based on a response matrix, where we plotted the probabilities $P(E_j^{\text{rec}}, E_i^{\text{true}})$ that an energy E_i^{true} was reconstructed as an energy E_j^{rec} (where $E_i^{\text{true}}/eV \in [10^{16}, 10^{19.5}]$, thereby covering the energy range of interest where such effects are important). To unfold the effects of fluctuations and infer the true energy spectrum, we then had to solve a system of equations as Eq. (B.1):

$$N^{\text{rec}}(j) = \sum_{i=1}^{N_{\text{bins}}} P(E_j^{\text{rec}}, E_i^{\text{true}}) N^{\text{true}}(i) \quad (\text{B.1})$$

where $\sum_{j=1}^{N_{\text{bins}}} P(E_j^{\text{rec}}, E_i^{\text{true}}) = 1$.

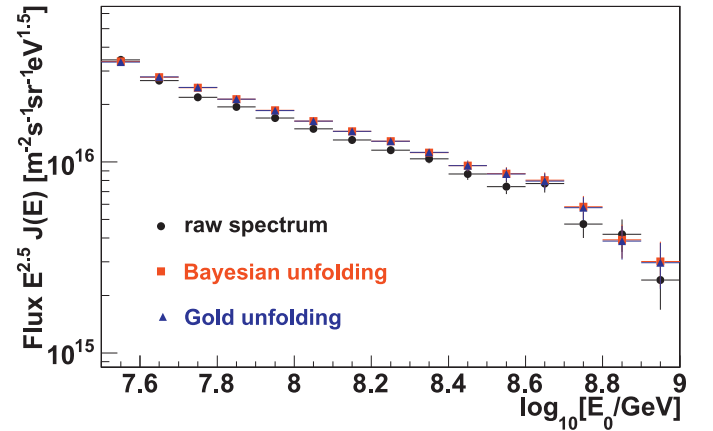


Fig. B.17. Results obtained by the Bayes and Gold unfolding algorithms.

The system was solved iteratively by applying a method based on the Gold algorithm [34] and the result was then compared with the result obtained by another approach based on the Bayes algorithm [35] (also applied iteratively). For a sufficiently large number of iterations, the results obtained by the two methods converged (Fig. B.17). For each unfolding procedure, a smoothing was applied to the result obtained from each intermediate iteration to avoid fluctuations amplifying from each iteration to the next. This smoothing was based on the 353HQ-twice algorithm [36]. In addition, the simulation-derived response matrix was smoothed in order to reduce the effects induced by the statistical fluctuations in the Monte Carlo sample. To smooth the response matrix, the information in each bin of true energy was fitted with a Gauss-Landau convolution and the parameters of the convolution function were then parameterized with the true energy.

The unfolding procedures based on the Gold and Bayes algorithms were tested by comparing the measured spectra with the forward folded ones and good agreement was observed.

Appendix C. Energy spectrum based on $S(500)$ and its systematic uncertainties

The experimental energy spectrum inferred from the proposed approach is shown as $E_0^{S(500)}$ in Fig. C.18 as well as the result obtained for KASCADE [26] toward lower energies, and the result obtained using the standard approach [7] as $E_0^{N_{\text{ch}}-N_\mu}$. It is important to note that the KASCADE spectrum was inferred from a procedure using the QGSJet-01 model for high energy interactions with

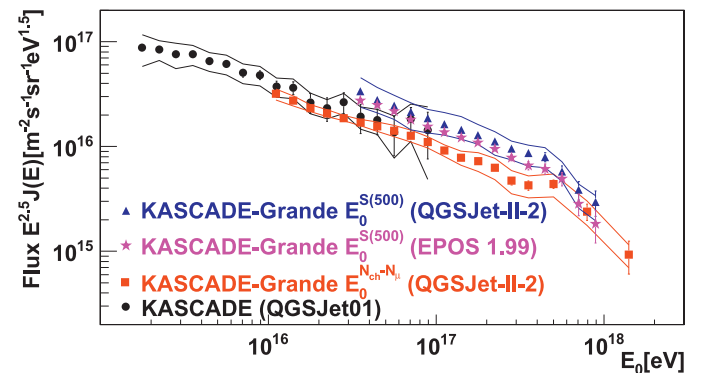


Fig. C.18. Primary energy spectra obtained for KASCADE [26] and KASCADE-Grande [7]. The bands with continuous lines show the estimated systematic uncertainty. In this plot, the $S(500)$ -derived energy spectra for KASCADE-Grande were inferred using calibrations based on simulations with QGSJet-II-2 and EPOS 1.99.

different specific systematics compared with the QGSJet-II-2 used to infer the two KASCADE-Grande spectra. The figure also shows the spectrum obtained when using EPOS 1.99 as the basis for calibration.

The reconstruction of energy from $S(500)$ relies on a considerable number of parameters, which can vary substantially on an arbitrary basis. By propagating through the calculus, these variations can lead to fluctuations in the flux obtained. We identified these free parameters and allowed them to vary within reasonable limits. The resulting variation in the energy flux (in %) was evaluated in each case.

- Accuracy of the $S(500)$ reconstruction

The $S(500)$ energy estimator was derived from a fit according to [25]. The quality of this fit was affected significantly by the number of stations as well as by their position inside the lateral density distribution. The fluctuations in the reconstructed $S(500)$ acted as a source of uncertainty and they amounted to $\approx 16.5\%$ at $E_0 = 10^{17}$ eV, where they decreased with energy to $\approx 8\%$ at $E_0 = 10^{18}$ eV [37].

- Uncertainties in the $E_0 - S(500)$ calibration

The simulation-derived calibration curve was obtained using a fitting procedure and each parameter was characterized by an uncertainty. In order to evaluate the effects of these uncertainties in terms of the systematics of the energy flux, the fit parameters were allowed to change according to their uncertainty and the primary energy spectrum was reconstructed in this particular new case. The contribution of this source was determined for a systematic uncertainty of $\approx 1\%$ at $E_0 = 10^{17}$ eV, where it increased with energy to $\approx 6\%$ at $E_0 = 10^{18}$ eV.

- Spectral index of the simulated event sample

The simulated shower sample used throughout this study was weighted on an event-by-event basis to emulate a primary energy spectrum with a spectral index $\gamma = -3$, which is close to the natural index of the cosmic ray spectrum but not exactly the same. The reconstruction was repeated for the cases where $\gamma = -2.8$ and $\gamma = -3.2$, and the difference between the fluxes obtained in these two cases was considered as systematic uncertainty. The source amounts for $\approx 2\%$ at $E_0 = 10^{17}$ eV increased slightly with energy to $\approx 4\%$ at $E_0 = 10^{18}$ eV.

- Influence of the Monte-Carlo statistics on the fitting parameters

The simulated shower sample used for energy calibration was generated by a Monte Carlo algorithm, which introduced various fluctuations with different energy ranges because the energy spectrum is a power law and far less events were available for analysis at high energies than lower energies. In order to estimate the effects of these fluctuations, the energy range was divided into three sub-ranges and the energy calibration was performed for every sub-range. The new parameterizations varied slightly among cases due to the Monte Carlo fluctuations. The reconstruction was performed for each particular parameterization and the results were compared. For every energy bin, the difference between the maximum reconstructed flux and the minimum value was defined as the systematic uncertainty from this source, which for $\approx 2\%$ at $E_0 = 10^{17}$ eV, increased with energy to $\approx 8\%$ at $E_0 = 10^{18}$ eV.

- Systematic error introduced by the CIC

The CIC (Appendix A) method provides an attenuation-corrected $S(500)$ with an associated uncertainty that results from the CIC method itself, which acts as another source of systematic uncertainty because the corrected $S(500)$ is converted to energy. To evaluate the contribution of the CIC method to the overall systematics, we allowed the corrected $S(500)$ value of each event to change according to the CIC-specific uncertainty. The contribution to the resulting energy flux was rather small at less than 1% over the entire energy range.

- Choosing a specific reference angle at which to perform the $S(500)$ correction of attenuation

A specific reference angle is selected when correcting the $S(500)$ for attenuation. The experimental zenith angular distribution peaked at 21° , so the reference angle was selected as 21° in order to ensure that the CIC method significantly affected as few showers as possible. However, it is possible to choose another angle without changing the relevance of the final result, but the correction would affect each shower in a different way depending on the choice of reference angle. As extreme cases, we selected reference angles of 0° and 30° , and we compared the resulting spectra after applying CIC for these reference angles. The difference between these spectra defined the contribution of this uncertainty source, which was $\approx 6\%$ at $E_0 = 10^{17}$ eV and it increased to $\approx 14\%$ at $E_0 = 10^{18}$ eV.

- Response matrix correction

The response matrix correction (see Appendix B) involved complex mathematical operations, which contributed to the final systematic uncertainties. To evaluate this contribution, test spectra were generated by introducing random Poisson noise in the raw un-corrected energy spectrum and then unfolding it. The test spectra were forward folded (the inverse operation of the unfolding procedure) and then re-unfolded. The average difference between the re-unfolded spectra and the average of the test spectra was used to define the contribution of the response matrix correction, which contributed about 4% over the entire energy range.

- Hadronic interaction model

The combination of QGSJet-II-2 and FLUKA models has been used in all studies of simulated events and it is expected that the model itself introduces a systematic effect when describing certain shower properties. To obtain a rough estimate of this systematic effect, a second calibration was been from simulations based on the EPOS 1.99 model and on average, the energy variation with the new calibration was systematically $\approx 10\%$ lower than that for QGSJet-II-2. Similarly, when we treated the EPOS shower sample as experimental data and reconstructed it using the calibration based on the QGSJet-II-2 model, we obtained a systematic $\approx 10\%$ overestimation of the energy. This contribution was only evaluated in this case, but it was not included in the systematic uncertainty band in Fig. C.18, Section 4.1.

The method-specific sources described above (excluding the hadronic interaction models) introduce a combined systematic uncertainty of $\approx 32\%$ in the energy flux at $E_0 = 10^{17}$ eV and it increased to $\approx 45\%$ at $E_0 = 10^{18}$ eV.

References

- [1] V. Berezhinsky, A. Gazizov, S. Grigorieva, *Phys. Rev. D* 74 (4) (2006) 043005.
- [2] A.M. Hillas, *J. Phys. G: Nucl. Part. Phys.* 31 (2005) R95.
- [3] Telescope Array Collaboration, *Astrophys. J.* 794 (2014) 172.
- [4] W.D. Apel, et al., *Nucl. Instrum. Methods A* 620 (2010) 202–215.
- [5] T. Antoni, et al. (KASCADE Collaboration), *Nucl. Instrum. Methods A* 513 (2003) 429.
- [6] M. Aglietta, et al. (EAS-TOP Collaboration), *Nucl. Instrum. Methods A* 336 (1993) 310.
- [7] W.D. Apel, et al. (KASCADE-Grande Collaboration), *Astropart. Phys.* 36 (2012) 183–194.
- [8] W.-D. Apel, et al. (KASCADE-Grande Collaboration), *Phys. Rev. Lett.* 107 (2011) 171104.
- [9] W.-D. Apel, et al. (KASCADE-Grande Collaboration), *Phys. Rev. D* 87 (R) (2013) 081101.
- [10] H.Y. Dai, et al., *J. Phys. G Nucl. Phys.* 14 (1988) 793.
- [11] A.M. Hillas, et al., Measurement of primary energy of air showers in the presence of fluctuations, in: *Proceeding of the 12th International Cosmic Ray Conference, ICRC, Hobart, vol. 3, 1971, p. 1001.*

- [12] H. Rebel, O. Sima, et al., Studies of different LDFs for primary energy estimation and mass discrimination of cosmic rays by the EAS lateral charged particle distribution as observed by KASCADE-Grande, in: Proceedings of the 29th International Cosmic Ray Conference, ICRC, Pune, India, vol. 6, 2005, p. 297; I.M. Brancus, et al., Event - by - event studies of the discriminative features of the LDF of charged EAS particles: observable correlations and nonparametric analyses of multivariate distributions, in: Proceedings of the 29th International Cosmic Ray Conference, ICRC, Pune, India, vol. 6, 2005, p. 361.
- [13] D. Heck, et al., CORSIKA: A Monte Carlo code to simulate extensive air showers, Report, vol. 6019, Forschungszentrum Karlsruhe, 1998.
- [14] N.N. Kalmykov, S.S. Ostapchenko, A.I. Pavlov, Nucl. Phys. B: Proc. Suppl. 52B (1997) 17–28; S.S. Ostapchenko, Nucl. Phys. B: Proc. 151 (2006) 143–147; S.S. Ostapchenko, Phys. Rev. D 74 (2006) 014026.
- [15] T.T. Böhlen, F. Cerutti, M.P.W. Chin, A. Fassò, A. Ferrari, P.G. Ortega, A. Mairani, P.R. Sala, V. Vlachoudis, The FLUKA code: developments and challenges for high energy and medical applications, Nucl. Data Sheets 120 (2014) 211–214.
- [16] A. Ferrari, P.R. Sala, A. Fassò, J. Ranft, FLUKA: A Multi-particle Transport Code. CERN-2005-10 (2005), INFN/TC_05/11, SLAC-R-773, 2005 (CERN, INFN and SLAC reports).
- [17] A. Gherghel-Lascu, et al., Effects of the new hadronic interaction models on the reconstruction of KASCADE-Grande observables, in: Proceedings of the 34th International Cosmic Ray Conference, ICRC, The Hague, Netherlands, 2015.
- [18] K. Werner, F.M. Liu, T. Pierog, Phys. Rev. C 74 (2006) 044902.
- [19] S. Ostapchenko, Phys. Rev. D 83 (2011) 014018.
- [20] T. Pierog, Iu. Karpenko, J.M. Katzy, E. Yatsenko, K. Werner, Phys. Rev. C 92 (2015) 034906.
- [21] O. Sima, et al., SHOWREC - A program for reconstruction of EAS observables from KASCADE-Grande observations, Report, vol. 6985, Forschungszentrum Karlsruhe, 2004.
- [22] F. Cossavella, et al., Electron shower size spectra reconstructed with KASCADE-Grande data, in: Proceedings 30th International Cosmic Ray Conference, ICRC, Merida, Mexico, vol. 4, 2007, p. 211; R. Glasstetter, et al., Shower size reconstruction at KASCADE-Grande, in: Proceedings of the 29th International Cosmic Ray Conference, ICRC, Pune, India, vol. 6, 2005, p. 293.
- [23] G. Toma, et al., A fast simulation procedure for calculating the energy deposits of charged particles in EAS observations, in: Proceedings of the 26th International Conference on ECRS, Lisbon, Portugal so-134, 2006; Application Software Group - Computing and Networks Division, GEANT Detector Description and Simulation Tool, CERN Program Library Long Writeup, 1997.
- [24] O. Sima, et al. (KASCADE-Grande Collaboration), Nucl. Instrum. Methods A 638 (2011) 147–156.
- [25] J. Linsley, et al., J. Phys. Soc. Jpn. 17 (1962) A–III.
- [26] T. Antoni, et al., Astrop. Phys. 24 (2005) 1.
- [27] W.-D. Apel, et al. (KASCADE Collaboration), Astrop. Phys. 24 (2006) 467.
- [28] R. Ulrich, et al. (Pierre Auger Collaboration), Phys. Rev. Lett. 109 (2012) 062002.
- [29] G. Antchev, et al. (TOTEM Collaboration), Phys. Rev. Lett. 111 (1) (2013) 012001; G. Antchev, et al., Europhys. Lett. 101 (2013) 21004.
- [30] J.C.A. Velázquez, (KASCADE-Grande Collaboration), et al., Tests of HE hadronic interaction models with the muon attenuation length in KASCADE-Grande, in: Proceedings of the 34th International Cosmic Ray Conference, ICRC, The Hague, Netherlands, 2015.
- [31] A. Aab, et al. (Pierre Auger Collaboration), Phys. Rev. D 91 (2015) 059901.
- [32] M. Roth, et al., Measurement of the UHECR energy spectrum using data from the surface detector of the Pierre Auger Observatory, in: Proceedings of the 30th International Cosmic Ray Conference, ICRC, Merida, Mexico, vol. 4, 2007, p. 327.
- [33] M. Nagano, et al., J. Phys. G Nucl. Phys. 10 (1984) 1295.
- [34] R. Gold, An iterative unfolding method for response matrices, Report ANL-6984, Argonne National Laboratory, Argonne, 1964; H. Ulrich, Primary energy spectra of cosmic rays selected by mass groups in the knee region, Proceedings of the 27th International Cosmic Ray Conference, ICRC, Hamburg, Germany, 2001.
- [35] G. D'Agostini, A multidimensional unfolding method based on Bayes' Theorem, DESY94-099, vol. 362, 1994; G. D'Agostini, 1995 NIMA, 362 487–498.
- [36] J. Friedman, Proc. of the 1974 CERN School of Computing, Norway, 1974, pp. 11–24.
- [37] O. Sima, et al., The reconstruction of the lateral charge particle distributions and the studies of different LDF parameterisations, in: FZKA Interner Bericht KASCADE-Grande 2005-01, Forschungszentrum Karlsruhe, 2005.